


Cite this: *J. Mater. Chem. A*, 2024, 12, 26132

# Imparting hydrophobicity to a MOF on layered MXene for the selective, rapid, and ppb level humidity-independent detection of NH<sub>3</sub> at room temperature†

Kugalur Shanmugam Ranjith,<sup>a</sup> Sonam Sonwal,<sup>b</sup> Ali Mohammadi,<sup>a</sup> Ganji Seeta Rama Raju,<sup>a</sup> Mi-Hwa Oh, <sup>\*c</sup> Yun Suk Huh <sup>\*b</sup> and Young-Kyu Han <sup>\*a</sup>

The sensitivity of chemiresistive sensors is inherently compromised by ambient humidity and trace level detection of toxic gases has potential challenges at room temperature. Herein, we designed a metal–organic framework (MOF) on a layered MXene hybrid by tagging a ZIF-67-based MOF on layered Ti<sub>3</sub>C<sub>2</sub>T<sub>x</sub> MXene and following this with a surface ligand exchange process to design a highly sensitive, humidity tolerant chemiresistive sensor for ultra-low ppb level (200 ppb) NH<sub>3</sub> sensing. The gas selectivity of MXenes was influenced by surface tagging with the MOF, which creates high surface-active features that promote the interaction and selectivity of NH<sub>3</sub> on the MXene surface. In addition, a passive shell ligand exchange reaction provides not only a hydrophobic surface and environmental stability to the hybridized surface but also contributes to the sensing performances. The hybridized H-MOF/MXene-based sensor exhibited a superior NH<sub>3</sub> sensing response ( $\Delta R/R_g = 6.9$ , 1 ppm) at room temperature with high selectivity and reliability and a theoretical detection limit of 12.8 ppb. Passive ligand exchange had a significant effect on the sensing response at room temperature but improved humidity resistance and long-term durability. The H-MOF/MXene response to NH<sub>3</sub> was only reduced by 0.22% and 0.27% at relative humidities of 76% and 93%, which represented 1.2 and 8.3-fold improvements in the sensing response versus MOF<sub>6</sub>/MXene and bare MXene at an NH<sub>3</sub> concentration of 10 ppm. Furthermore, the sensing mechanism involved electronic interactions and charge transfer through a Schottky junction between the MOF and MXenes and the synergistic promotion of the sensing response on the hybridized H-MOF/MXene platform. This work provides a means of designing a surface functionalized MOF on MXene heterostructures that enables the production of sensors tailored to diverse environmental conditions.

Received 5th July 2024  
Accepted 26th August 2024

DOI: 10.1039/d4ta04656k

rsc.li/materials-a

## 1 Introduction

NH<sub>3</sub> is a significant pnictogen hydride and irritant that is widely used in the automotive, agrochemical, petrochemical, beverage, and dairy industries.<sup>1</sup> Annual demand for NH<sub>3</sub> exceeds 145 million tons with a market value of ~70 billion USD. Furthermore, global demand is accelerating, which increases concerns about NH<sub>3</sub> released into the environment<sup>2</sup> because NH<sub>3</sub> and related pollutants adversely affect air quality and can cause

visual impairment on contact and serious damage to the human nervous and respiratory systems. Low-cost, highly accurate analytical tools are required for NH<sub>3</sub> detection in the medical, food processing, fertilizer manufacturing, and animal husbandry sectors because of the high cost and inconvenience of analytical techniques, such as chemiluminescence and gas chromatography.<sup>3</sup> Recently, NH<sub>3</sub> detection has been facilitated by the advent of metal oxide-based chemiresistive sensors because of their exceptional sensitivity and real-time capabilities.<sup>4,5</sup> However, selectivity and high operation temperatures (70–400 °C) have limited the practical utilities of metal oxide-based sensors that rely on oxygen species generated at high temperatures.<sup>6,7</sup> Furthermore, developing a sensor for room-temperature use has significant impacts on device power consumption and safety, and wearable sensors are likely to replace traditional sensors.<sup>8,9</sup> Material design plays a crucial role in fabricating room-temperature-based sensors for detecting harmful gases by dictating the dimensions and

<sup>a</sup>Department of Energy and Material Engineering, Dongguk University-Seoul, Seoul 04620, Republic of Korea. E-mail: ykenergy@dongguk.edu

<sup>b</sup>Department of Biological Sciences and Bioengineering, Nano Bio High-Tech Materials Research Center, Inha University, 100 Inha-ro, Michuhol-gu, Incheon 22212, Republic of Korea. E-mail: yunsuk.huh@inha.ac.kr

<sup>c</sup>National Institute of Animal Science, Rural Development Administration, Wanju 55365, Republic of Korea. E-mail: moh@korea.kr

† Electronic supplementary information (ESI) available. See DOI: <https://doi.org/10.1039/d4ta04656k>



compositions of semiconducting nanostructures.<sup>10</sup> MXene-based nanostructures are interesting two-dimensional (2D) platforms derived from MAX by Al etching.<sup>11</sup> These nanostructures have excellent chemical, physical, and electronic properties and are mechanically stable and highly hydrophilic, which has promoted interest in their use for gas adsorption.<sup>12</sup> A variety of MXenes [ $M_{n+1}C_nT_x$  ( $M = \text{Ti, V, Mo, Nb, Cr, etc.}$ )] have been investigated as potential sensor materials for the detection of different VOCs, such as ethanol, acetone, formaldehyde,  $\text{NH}_3$ ,  $\text{NO}_2$ , and hydrogen sulfide.<sup>13</sup> Nevertheless, the poor stability of MXenes in humid environments restricts their long-term usage since partial surface oxidation in humid environments reduces their conductivities.<sup>14</sup> Various strategies have been devised to eliminate surface oxidization by modifying MXene surfaces, such as removing hydroxy groups and increasing surface hydrophobicity.<sup>15</sup> However, although these strategies protected MXene surfaces from oxidation, the sensors produced had selectivity shortcomings.<sup>16</sup> Different strategies, such as increasing surface functionality, have been investigated to improve the selectivity of MXene sensors without compromising their sensing abilities.<sup>17,18</sup>

The design of metal–organic frameworks (MOFs) on MXene surfaces has shown promise in terms of maximizing sensitivity by increasing adsorption capacity, surface area, electronic interactions, and substrate porosity.<sup>19,20</sup> MOFs are metal-coordinated cationic polymer nanomaterials consisting of metal nodes and organic linkers, and in addition to the advantages mentioned above, MOFs have low environmental toxicities.<sup>21</sup> However, the inferior conductivity and poor response recoverability of MOFs limit their sensitivities in chemiresistive gas sensors.<sup>22</sup> MOF-derived metal compositions or tagged MOF heterostructures are generally preferred as chemiresistive sensors due to their high adsorption capacities and porous nature, which maximize active sites.<sup>23,24</sup> Zeolitic imidazolate framework (ZIF) based metal–organic frameworks have a high selectivity towards  $\text{NH}_3$  adsorption, through the selective pore size and acid–base interaction within the zeolite groups.<sup>25</sup> Meanwhile, surface tagging of a MOF on a 2D layered surface prevents self-aggregation, maximizes surface-active sites, and favors high sensitivity.<sup>26</sup> Tagging MXenes with MOFs was found to provide a more effective platform than other semiconducting compositions and to serve as a heterostructure interface with a Schottky junction that promoted gas molecule-induced resistance changes and combined these with the advantages of high conductivity and effective carrier transportation.<sup>27</sup> The heterostructure assembly of MOFs on MXene templates is made possible by hydrogen bonding or electrostatic interactions that create a Schottky junction at the metal–semiconductor interface.<sup>28</sup> To address the challenges of humidity-independent  $\text{NH}_3$  detection at room temperature (RT), the MOF on MXene hybrids needs to have good electrical conductivity and humidity-tolerant surface functionality. Reducing water affinity, enhancing moisture stability, and designing highly porous hydrophobic MOFs have led to a unique class of applications.<sup>29</sup> The strategies used to fabricate hydrophobic MOFs involve ligand design and post-synthetic hydrophobization.<sup>30</sup> However, despite its improved stability,

specific surface areas and surface-active sites were diminished and parent properties were somewhat impaired due to capping functionalities that enhanced the hydrophobic nature of the MOF.<sup>31</sup> Coupling MOFs and MXenes with the excellent heterostructure feature has promoted widespread application in electrochemical sensors.<sup>32,33</sup> Building a porphyrin-based MOF on MXenes achieved superior sensitivity for  $\text{NO}_2$  sensing with a high response ( $R_a/R_g = 2.0$ , 10 ppm) at RT, high reliability, and a low particle limit of detection (pLOD, 200 ppb).<sup>19</sup> Furthermore, a Co-TCPP(Fe)/ $\text{Ti}_3\text{C}_2\text{T}_x$  Schottky junction promoted electron transfer to provide outstanding selectivity and  $\text{Fe-N}_4$  functionality. Naveen *et al.*<sup>25</sup> reported the preparation of  $\text{Ti}_3\text{C}_2\text{T}_x$  with a mixed matrix membrane filter as a chemiresistive sensor for  $\text{NH}_3$  sensing at RT with a pLOD of 1 ppb. So far, dual enhancement towards the selectivity and anti-humidity properties on chemiresistive sensors based on MOF–MXene hybrids at room temperature has not been reported.

In this work, a hydrophobic MOF (H-MOF) on MXenes ( $\text{Ti}_3\text{C}_2\text{T}_x$ ) was specifically produced using a two-step fabrication strategy. First, thin-layered 2D MXene was prepared using a LiF/HCl-based acid etching process, and this was followed by delamination to produce extremely thin few layered sheets. Second, ZIF-67 tagged over MXenes *in situ* by hydrogen bonding was subjected to the shell ligand-exchange reaction (SLER) process. Tagging the MOF on the MXene surface promoted high selectivity towards  $\text{NH}_3$  through the effective adsorption due to selective pore size and acid–base interaction within the zeolite groups. Furthermore, the outer shell of ZIF-67 was modified to promote humidity tolerance without sacrificing its morphology or sensing performance. The designed H-MOF/MXene-based sensor exhibited superior sensing performance ( $\sim 8.3$  times that of pristine MXenes; ranging from 200 ppb to 50 ppm) towards  $\text{NH}_3$  at RT coupled with a low LOD (12.8 ppb), high response, selectivity, and humidity-independent  $\text{NH}_3$  detection. The sensing mechanism responsible for this superior  $\text{NH}_3$  response was attributed to (i) presence of a MOF on the MXene surface alters the electrical conductance upon uptake of analyte gas, and due to the molecular sieving effect, the MOF shows a high interaction towards  $\text{NH}_3$  that promotes the selectivity of the sensing device; (ii) charge transfer from the MOF to the MXene hybrid was made possible by the formation of a Schottky junction, which decreased the band gap and Fermi level of ZIF-67 in the vicinity of MXenes; and (iii) surface passivation by organic functionality, which promoted hydrophobicity and minimized interface contact with OH functionalities, facilitating humidity-independent  $\text{NH}_3$  detection. The dramatic synergistic effects of gas adsorption and charge transportation on the MOF on MXenes provide clues regarding the potential sensing applications of MXene-based sensors.

## 2 Experimental section

### 2.1 Synthesis of few-layered MXene nanosheets

Typically, 1 g of lithium fluoride (LiF, 99.9% Sigma Aldrich, USA) was added to 20 mL of 9 M hydrochloric acid (HCl, 37%, DAEJUNG, South Korea) and stirred for 10 min.  $\text{Ti}_3\text{AlC}_2$  MAX (1 g; Carbon, Ukraine) was then gradually added and stirred for



72 h at 40 °C. The resulting material was repeatedly suspended in distilled (DI) water and centrifuged until it reached a pH of 6.0. The final suspension was ultrasonicated, and centrifuged at 5000 rpm for 5 min; the supernatant was collected, freeze-dried, and later subjected to the delamination process. Briefly, 100 mg of freeze-dried MXene was dispersed in 40 mL of dimethyl sulfoxide (DMSO, >99.9%, DAEJUNG, South Korea) under constant stirring for 12 h, redispersed in 40 mL of DI water, sonicated for 4 h in an ice bath in an Ar atmosphere, and centrifuged at 3000 rpm for 10 min. The supernatant nano-sheets were then collected, freeze-dried, and used to create the hybrid heterostructure. All reagents used in the work were used without further purification.

## 2.2. Synthesis of ZIF-67/MXene

Pristine ZIF-67 (a type of MOF) was prepared at RT using 1 mmol of cobalt nitrate hexahydrate ( $\text{Co}(\text{NO}_3)_2 \cdot 6\text{H}_2\text{O}$ , >99.9%, Sigma Aldrich, United Kingdom) and 4 mmol of 2-methylimidazole (2-MIM, 99%, Sigma Aldrich, India).<sup>34</sup> To ensure intimate contact between the MOF and the MXene surface, the MXene surface was nucleated with Co ions before growing the MOF on MXene. Few-layered MXene (100 mg) was dispersed in 20 mL of methanol, and 10 mg of  $\text{Co}(\text{NO}_3)_2 \cdot 6\text{H}_2\text{O}$  was then dissolved in this dispersion by stirring for 2 h. The dispersion was then centrifuged and dried at 110 °C under vacuum for 2 h. To grow the MOF on the MXene surface, 100 mg of Co-nucleated few-layered MXene was dispersed by ultrasonication in 25 mL of methanol for 30 min. 22 mg of  $\text{Co}(\text{NO}_3)_2 \cdot 6\text{H}_2\text{O}$  and the mix were stirred for 3 h to increase the Co ion nucleation on the MXene surface. 25 mL of 2-MIM (79 g) solution was then slowly added to this MXene dispersion and stirred at 150 rpm to avoid sedimentation. The mixture was aged at RT for 6 h to allow the ZIF-67/MXene heterostructure to form. Finally, it was dried at 60 °C in a vacuum for >6 h and labeled as a MOF on MXene. The loading density of the MOF on MXene was investigated by increasing the  $\text{Co}(\text{NO}_3)_2 \cdot 6\text{H}_2\text{O}$ /2-MIM concentration at a constant amount of MXene. The samples were named  $\text{MOF}_x/\text{MXene}$  ( $x = 2, 4, 6, 8$ , and 10 wt%), where 'x' indicates MOF loading density. Increasing MOF loading density was found to reduce the conductivity of the MXene heterostructure and reduce sensing performance on high loading of the MOF on the MXene surface.

## 2.3. Synthesis of hydrophobic ZIF-67/MXene using the SLER process

The SLER was performed as previously described.<sup>35</sup> Prepared ZIF-67/MXene (0.2 g) heterostructures were dispersed in methanol (MeOH, >99.8%, DAEJUNG, South Korea) with triethylamine (TEA, >99%, DAEJUNG, South Korea) and 5,6-dimethylbenzimidazole (DMBIM, Sigma Aldrich, Germany) (weight composition: ZIF-67/MXene : DMBIM : TEA : MeOH = 1 : 1 : 0.7 : 150) and stirred for 12 h at 60 °C. The final product was washed with methanol, dried under vacuum for 6 h, and stored in a desiccator until required. After the SLER process, ZIF-67 was termed H-ZIF-67, which retained the original crystal structure of ZIF-67 but had a remarkable hydrophobic nature

and similar sensing ability. A similar experimental process was performed to prepare H-ZIF-67, except that MXenes were omitted. The DMBIM concentration was optimized to create a thin, water-repellent surface with high sensor selectivity.

## 2.4. Materials characterization

High-resolution scanning electron microscopy (HRSEM, S-4800; Hitachi) and field emission transmission electron microscopy (FETEM, JEM-2100F; JEOL Japan) coupled with energy dispersive spectroscopy (EDX) were used to conduct the structural, morphological, and compositional analyses of the MXene hybrid. X-ray diffraction (XRD, PANalytical X'Pert Pro multi-purpose X-ray diffractometer with Cu K $\alpha$  diffraction ( $\lambda = 1.54 \text{ \AA}$ )) and Raman spectroscopy (FEX, NOST; Republic of Korea equipped with a 532 nm laser) were used to investigate the structures of the MOF, MXene, and MXene hybrid. Fourier transform infrared spectroscopy (FTIR, JASCO FTIR 6600) was used to investigate functionalities, and X-ray photoelectron spectroscopy (XPS, Thermo Scientific, Al K $\alpha$ , 1486.6 eV) was used to collect information about the composition and electron states of MXene heterostructures. The specific surface areas of nanostructures were measured using a Brunauer–Emmett–Teller (BET, Tristar ASAP 2020) gas sorption analyzer at 77 K. The hydrophobic nature of the samples was assessed by measuring contact angles on sample films. Optical absorption and band gaps of the samples were quantified by UV-vis diffused reflectance spectroscopy (UV-vis DRS, JASCO V-600).

## 2.5. Gas sensor fabrication and sensing measurements

The samples were loaded on an Au interdigitated electrode (IDE) deposited on a  $\text{SiO}_2$  substrate using the drop and dry method, *i.e.*, 2  $\mu\text{L}$  of the sample dispersed in ethanol (10 mg  $\text{mL}^{-1}$ ) was drop-coated and dried at 60 °C for 2 h in a vacuum. The gas sensing performances of prepared sensors were tested in a closed chamber (Nextron microprobe system) at RT (25 °C). The sensing signal was obtained from a Keithley 2400 coupled with NEXTRON software at a constant voltage of 0.2 V throughout the testing process using compressed air as a carrier gas with different concentrations of  $\text{NH}_3$  which were made using mass flow controllers (MFCs). To determine sensor selectivity,  $\text{NH}_3$  was replaced with carbon dioxide ( $\text{CO}_2$ ), triethylamine, ethanol, or acetone under the same conditions. The humidity of the sensing chamber was maintained at 51% for all sensing measurements to study the sensing abilities of different MXene-based hybrids. Sensing chamber RH was controlled between 10 and 93% using a homemade gas line system. The humidity of the test gas was calibrated using a commercial humidity sensor inside the chamber. The sensing performance of the built-in sensor was studied at different temperatures and RHs to quantify the sensitivity and durability of the sensing surface. For n-type behavior, the response ( $R\%$ ) to the target gas was defined as  $[(R_a - R_g)/R_g] \times 100\%$ . For p-type behavior, the response ( $R\%$ ) to the target gas was defined as  $[(R_g - R_a)/R_a] \times 100\%$ , where  $R_a$  and  $R_g$  are the sensor resistance in the presence of air and the target gas, respectively. Responses at different relative humidity levels ( $S_h$ ) were quantified using:



$$S_h = \frac{R_a}{R_h} \quad (1)$$

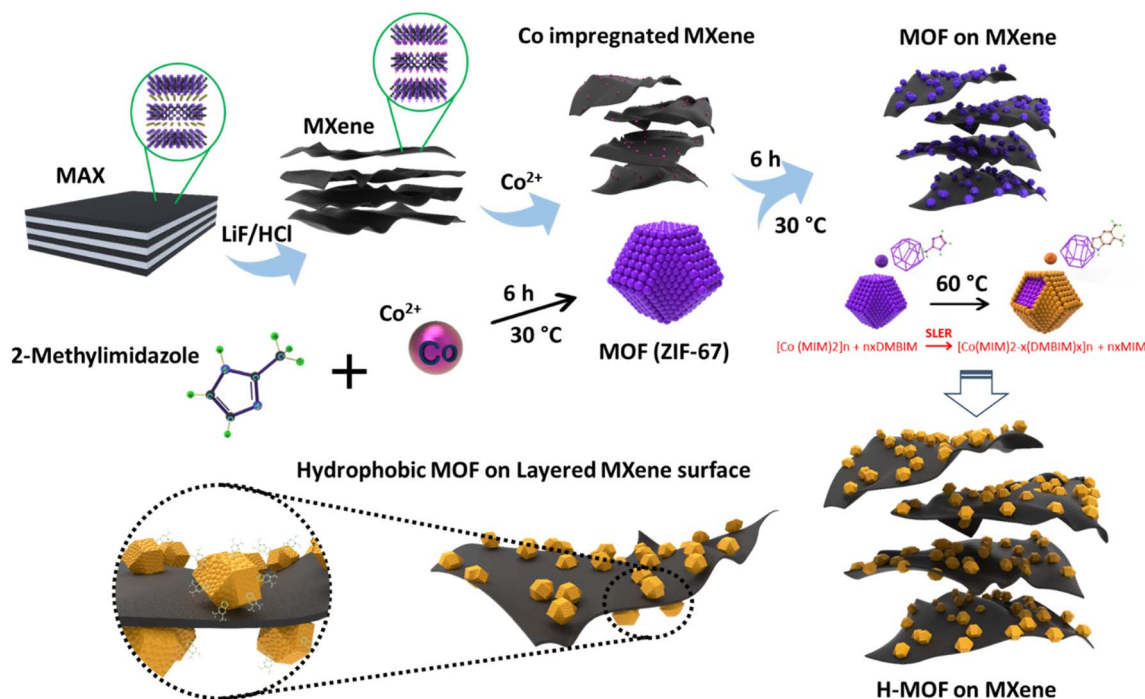
where  $R_h$  is the sensor resistance in a humid atmosphere. The response and recovery times were defined by the times needed to achieve 90% of electrical resistance during adsorption and desorption.

### 3 Results and discussion

Layered MXene was fabricated by selectively removing Al layers from  $\text{Ti}_3\text{AlC}$  MAX using  $\text{HCl/LiF}$  solution as the etchant, followed by a delamination process to prepare few-layered MXene sheets. Scheme 1 illustrates the synthesis of polyhedral ZIF-67 with surface ligand exchange of DMBIM on few-layered MXene as a hybrid assembly. ZIF-67 was prepared from 2-methylimidazole and  $\text{Co}(\text{NO}_3)_2 \cdot 6\text{H}_2\text{O}$  using a methanol-assisted solvent phase at RT, and DMBIM was modified using the SLER process. Co ionic nucleates were initially tagged over the MXene surface as a seeding platform to promote the growth of MOFs. A MOF on MXenes was prepared by growing polyhedral ZIF-67 nanostructures on the MXene surface and surface capping with DMBIM to create a hydrophobic hybrid structure. The detailed synthesis is provided in the Experimental section.

The selective etching of Al in MAX to form MXenes was verified by XRD (Fig. S1†). Effective removal of the (104) plane with the mild shift in the (002) plane representing increased  $d$ -spacing, confirmed the formation of MXenes. SEM images of  $\text{Ti}_3\text{C}_2\text{T}_x$  MXene are provided in Fig. 1a and S2.† EDAX spectra confirmed the presence of Ti, C, F, O, and Cl and a minimal amount of Al compared to the MAX phase. TEM (Fig. S2†) confirmed the fabrication of few-layered MXene and confirmed

a lattice spacing of 0.23 nm representing the crystal plane of MXenes (0110).<sup>36</sup> The detailed morphologies of H-ZIF-67 and H-MOF<sub>6</sub>/MXene (6 wt% of MOF : MXene) are shown in Fig. 1. The SEM images in Fig. 1b and c show the polyhedral morphology of H-ZIF-67 nanostructures and a particle size of ~900 nm. High-magnification images showed that the rough surface features of H-ZIF-67 may have been caused by DMBIM surface capping during the SLER process; these features were not observed in pristine ZIF-67 (Fig. S3†). No other significant change in the morphology or size of ZIF-67 was attributed to DMBIM. Fig. 1d and e show the distribution of polyhedral nanostructures on the layered MXene surface, indicating surface tagging of H-ZIF-67 on MXenes. The intimate contact between the MOF and MXene might have been due to the surface nucleation of Co ions on MXenes. In the absence of a nucleation process, ZIF-67/MXene was a composite structure composed of a random distribution of MXenes and micro-structured ZIF-67 (Fig. S4†). Initial seeding of Co on MXenes maximized the interaction of ZIF-67 nucleates on the layered MXene surface and promoted the growth of ZIF-67 on the MXene surface. Furthermore, this interaction may have promoted Schottky junction formation. More information on this structural interface was obtained by TEM and image mapping analysis (Fig. 1f and g). Fig. 1f shows the intimate contact between MXenes and H-ZIF-67, which was impregnated into the layered surface. TEM mapping and EDX spectra demonstrated that Ti, C, O, and F were uniformly distributed on the layered surface. Meanwhile, Co ions were distributed in certain areas, indicating the successful preparation of a MOF on the MXene hybrid. Increasing the Co/2-MIM concentration during ZIF growth increased the density of the MOF on MXenes (Fig. S5†), but high MOF loadings on MXenes



**Scheme 1** Schematic illustration of the preparation of a hydrophobic MOF on the MXene hybrid heterostructure.





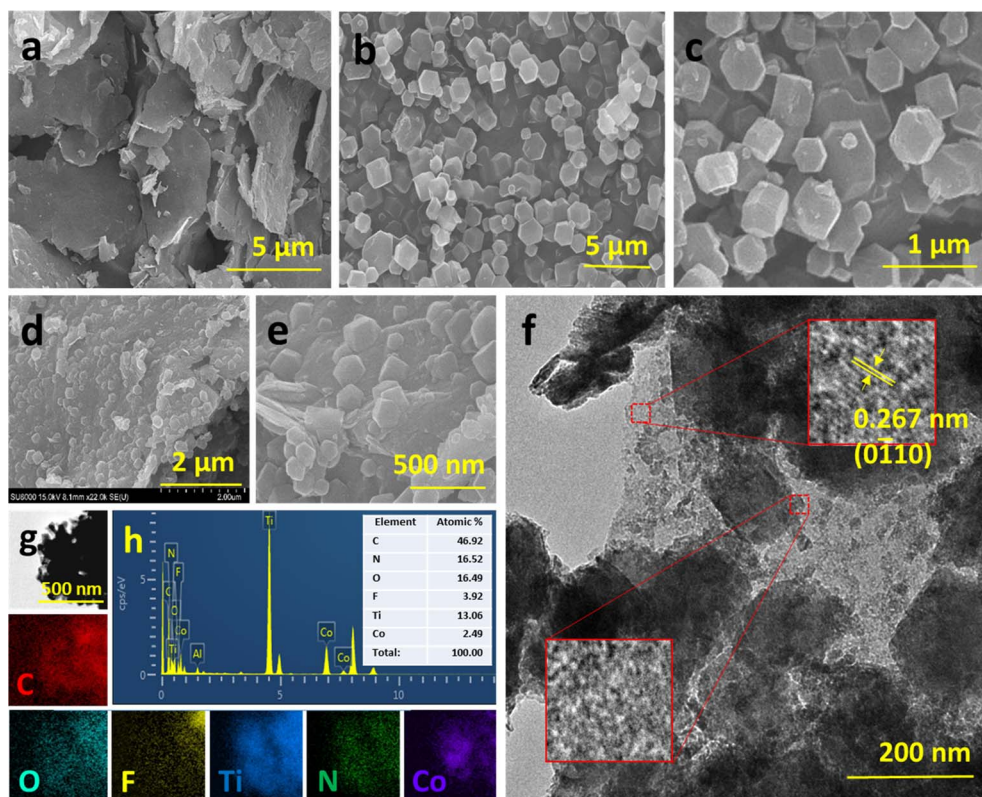


Fig. 1 SEM images of (a) MXenes, (b and c) H-ZIF-67, and (d and e) H-MOF<sub>6</sub>/MXene. (f) TEM (the inset shows HRTEM images of the MOF on MXenes), (g) TEM elemental mapping, and (h) EDAX spectra of H-MOF<sub>6</sub>/MXene for Ti, C, F, O, N, and Co.

resulted in an increase in the resistance of the hybrid surface and reduced the sensing ability of the hybrid layer surface (Fig. S6†). As MOF<sub>6</sub>/MXene exhibited excellent sensing response with stability and selectivity, it was considered the optimum sample and used for subsequent sensing-related experiments.

The structural and surface characteristics of the MXene hybrid were investigated by XRD, FTIR, Raman spectroscopy, and XPS (Fig. 2). The structures of ZIF-67, MOF<sub>6</sub>/MXene, and H-MOF<sub>6</sub>/MXene were analyzed by XRD (Fig. 2a). The XRD pattern of polyhedral ZIF-67 showed diffraction peaks at 7.3°, 10.3°, 12.6°, 16.3°, 17.9°, 22.1°, and 26.5°, which correspond to the (011), (002), (112), (013), (222), (114) and (134) planes, respectively, on the standard JCPDS card on ZIF-67 (67-1073).<sup>37</sup> The XRD pattern of the delaminated MXene showed the down shift of the (002) peak from 9.6° to 7.9°, resulting in the formation of MXenes with extended interlayer spacing (Fig. S1†). Heterostructure samples produced the combined diffraction peaks of ZIF-67 and MXenes. The interaction of the MOF on the MXene surface further downshifted the (002) peak of MXenes towards 6.3°, leading to the extended *d*-spacing of MXenes. It is worth noting that there is no significant peak shift between MOF<sub>6</sub>/MXene, and H-MOF<sub>6</sub>/MXene, suggesting that the crystal structure was not altered during the functionalization process. DMBIM-capping of heterostructures did not alter diffraction peaks, and neither did DMBIM functionalization of ZIF-67 (Fig. S7†). FTIR results for MXene, H-ZIF-67, MOF<sub>6</sub>/MXene, and H-MOF<sub>6</sub>/MXene heterostructures are shown in Fig. 2b.

Vibration peaks at 427 and 1576 cm<sup>-1</sup> were ascribed to Co-N and C=N stretching modes, respectively, and indicated the presence of metal-organic linker-based interactions. For MXenes and MXene heterostructures, vibrations of -OH, C-F, and Ti-O were attributed to peaks at 3425, 1066, and 559 cm<sup>-1</sup>, respectively.<sup>38</sup> Peaks observed between 900 and 1400 cm<sup>-1</sup> corresponded to the bending and stretching modes of C-H bonds in MOF-related samples, respectively. A comparison of the FTIR spectra of pristine and DMBIM-functionalized samples (Fig. 2b and S8†) showed the addition of peaks at 1233 and 854 cm<sup>-1</sup>, which corresponded to C-N stretch and C-H out-of-plane deformation vibrations of the phenyl rings of DMBIM, respectively.<sup>35</sup> The chemical structure and bonds between MXenes and ZIF-67 were investigated using Raman spectra (Fig. 2c). MOF<sub>6</sub>/MXene produced the characteristic of MXenes in the range of 100 to 800 cm<sup>-1</sup>. Peaks at 153 and 390 cm<sup>-1</sup> were assigned to plasmonic resonance, and in-plane vibrations of Ti-C (E<sub>g</sub>) and O (E<sub>g</sub>). Peaks at 265 and 617 cm<sup>-1</sup> represented A<sub>1g</sub> vibrations derived from the out-of-plane shearing modes of Ti-C (A<sub>1g</sub>) of H and C, respectively.<sup>39</sup> ZIF-67-based samples had peaks in the lower Raman shift region attributed to Co ions in ZIF-67.<sup>40</sup> Peaks at 421 and 673 cm<sup>-1</sup> were assigned to the Co-N and 2-MIM-based functional states.<sup>41</sup> Specifically, the band at 519 cm<sup>-1</sup> was assigned to the α-Co(OH)<sub>2</sub> stretch on the surface of ZIF-67. This band was not observed for H-ZIF-67, which was probably due to surface functionality removal by ligand exchange. On the other hand,



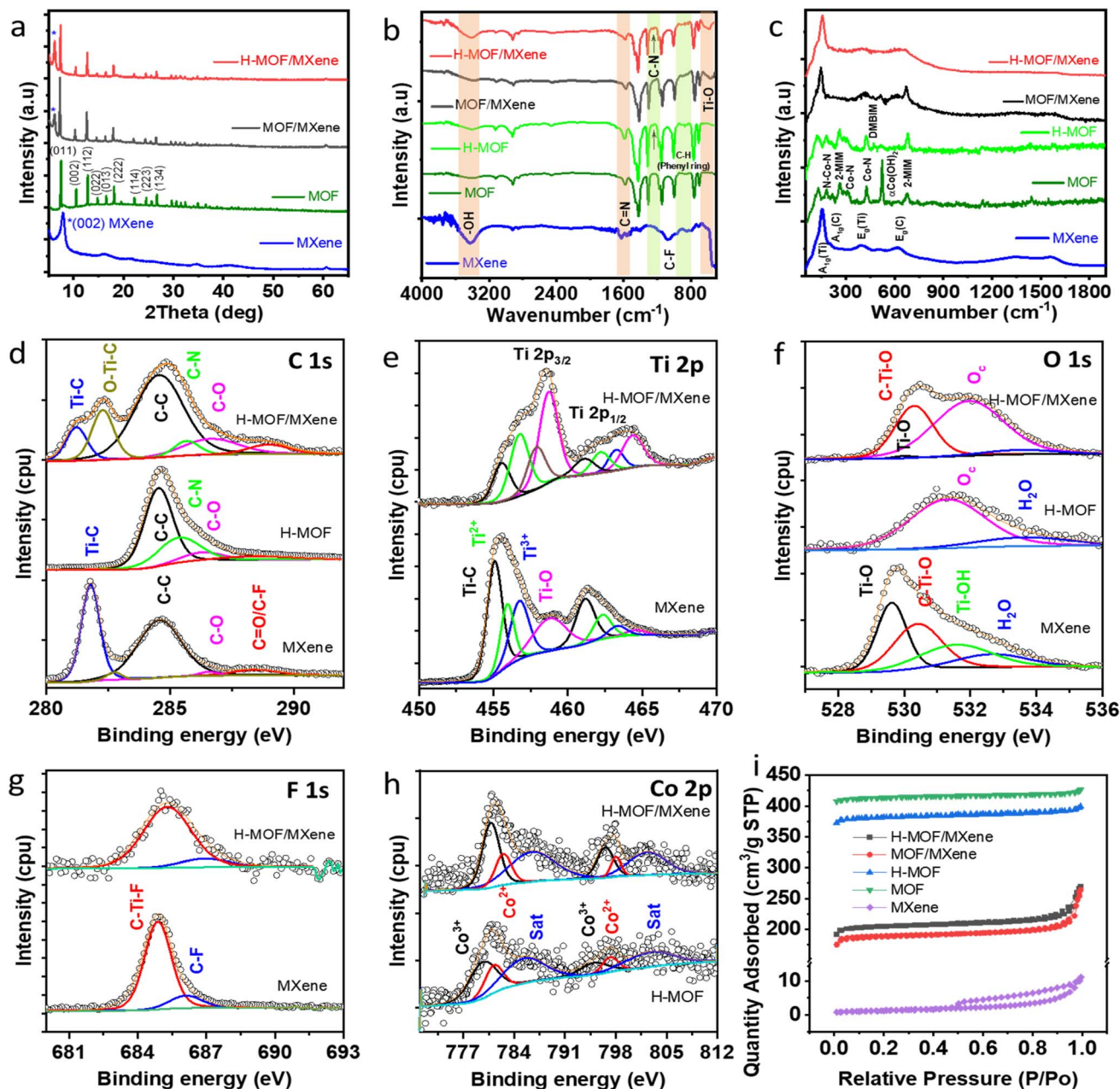


Fig. 2 (a) XRD, (b) FTIR, and (c) Raman spectra of MXenes, H-ZIF-67, MOF<sub>6</sub>/MXene, and H-MOF<sub>6</sub>/MXene. (d) C 1s, (e) Ti 2p, (f) O 1s, (g) F 1s, and (h) Co 2p XPS high-resolution spectra of MXenes, H-MOF, and H-MOF<sub>6</sub>/MXene. (i) N<sub>2</sub> adsorption-desorption analysis of MXenes, ZIF-67, MOF<sub>6</sub>/MXene, and H-MOF<sub>6</sub>/MXene.

a new peak at 470 cm<sup>-1</sup> was assigned to the in-plane deformation vibration of the fused rings of DMBIM on SLER-treated samples.

XPS was used to determine the electronic states and compositions of the as-prepared heterostructures. Survey spectra of MXenes and the heterostructures (Fig. S9†) provided C, Ti, O, F, N, and Co compositions. The high-resolution C 1s spectra of the MXene, H-ZIF-67, and H-MOF<sub>6</sub>/MXene are shown in Fig. 2d. Pristine MXene produced four peaks at 281.6, 284.6, 286.4, and 288.9 eV, which were attributed to C-Ti, C-C, C-N, C-O, and C=O/C-F, respectively. After ZIF-67 tagging, new

peaks were observed at 282.3 and 285.4 eV, which represented O-Ti-C and C-N, with a mild peak shift at 281.2 (Ti-C) for H-MOF<sub>6</sub>/MXene, confirming surface modification. As Fig. 2e shows, Ti 2p of pristine MXene produced peaks at 455.1, 456.1, 456.8, and 458.9 eV corresponding to Ti-C (Ti<sup>+</sup>), Ti-X (Ti<sup>2+</sup>), Ti-X (Ti<sup>3+</sup>), and Ti-O (Ti<sup>4+</sup>) at Ti 2p<sub>3/2</sub>, respectively. Ti-X was related to sub-stoichiometric titanium carbide and titanium oxycarbide functionalities. MOF tagging of MXenes resulted in Ti-O and 2-MIM-based interactions on the MXene and intense Ti-X and Ti-O-related peaks. The high-resolution O 1s spectra (Fig. 2f) of pristine MXene exhibited four peaks at 529.6, 530.4, 531.6, and



532.8 eV, which were attributed to Ti–O, C–Ti–O<sub>x</sub>, C–Ti–OH<sub>x</sub>, and C–O, respectively. Tagging of MXenes with the MOF also resulted in an intense peak at 531.8 eV, representing surface-adsorbed oxygen. A slight shift in the O 1s spectra of H-MOF<sub>6</sub>/MXene heterostructures resulted from a strong interaction between the MOF and the MXene surface. F 1s spectra of pristine MXene were attributed to Ti–F and C–F peaks at 684.3 and 685.9 eV, which was consistent with previous reports (Fig. 2i).<sup>18</sup> The F 1s spectrum of MOF<sub>6</sub>/MXene was downshifted to 685.3 eV, which was attributed to intimate contact between the –COOH functionality of MOF and F atoms on the MXene surface. N 1s spectra (Fig. S10†) confirmed the presence of pyridinic-N, pyrrolic-N, and graphitic-N functionalities on the MOF and H-MOF<sub>6</sub>/MXene samples. Due to the intimacy of the interaction between the MOF and MXene in H-MOF<sub>6</sub>/MXene, peak positions were shifted to lower binding energy with dense oxidation-N energy states. The Co 2p peaks of H-MOF and H-MOF<sub>6</sub>/MXene-based heterostructures are shown in Fig. 2j. Pristine ZIF-67 had two split peaks at 780.13/795.09 eV and 781.6/797.5 eV, which were ascribed to the Co<sup>3+</sup> and Co<sup>2+</sup> electronic states and corresponding satellite peaks at 785.8 and 802.9 eV. Compared to ZIF-67, the H-MOF<sub>6</sub>/MXene-based heterostructures showed a slight positive shift in binding energy, signifying electron transfer from the MOF to MXene. The surface area and the pore size distribution of MXenes and ZIF-67/MXene were obtained by BET analysis (Fig. 2k). The N<sub>2</sub> absorption–desorption isotherm represented a type 1a isotherm for the H-MOF<sub>6</sub>/MXene hybrid with a BET surface area of 812.44 m<sup>2</sup> g<sup>−1</sup> and a micropore volume of 0.1217 cm<sup>3</sup> g<sup>−1</sup>. The surface areas of ZIF-67 (1656.11 m<sup>2</sup> g<sup>−1</sup>) and H-ZIF-67 (1488.96 m<sup>2</sup> g<sup>−1</sup>) showed a minimal decrease in BET surface area and pore volume after the SLER process. The MOF<sub>6</sub>/MXene hybrid had a slightly higher specific surface area (755.95 m<sup>2</sup> g<sup>−1</sup>) and pore volume (0.1346 cm<sup>3</sup> g<sup>−1</sup>) than the H-MOF<sub>6</sub>/MXene hybrid because the DMBIM treatment reduced the porosity of the ZIF-67 surface. Nonetheless, the exposed pore volume of H-MOF<sub>6</sub>/MXene, which was greater than that of the pristine MXene nanosheets, was sufficient to facilitate rapid gas adsorption.

The gas sensing performances of MXenes, ZIF-67, MOF<sub>6</sub>/MXene, H-MOF<sub>6</sub>/MXene, and physically mixed MXene/H-ZIF-67 (10 : 1) composites were investigated at RT using compressed air as a carrier gas and different target gases. Over the interdigitated Au electrode, the MXene-based sensor exhibited a thickness of around 35 μm within an area of 0.5 × 0.5 cm (Fig. S11†). Fig. 3a shows gas responses over different MXene-based heterostructures to 10 ppm of NH<sub>3</sub>. Pristine MXenes produced a response of 1.37% to 10 ppm of NH<sub>3</sub>. Pristine H-ZIF-67 and physically mixed MXene/H-ZIF-67 nanocomposite sensors were not sensitive at RT because of their large resistances or insulating characteristics. MOF<sub>6</sub>/MXene and H-MOF<sub>6</sub>/MXene sensors exhibited responses of 8.73% and 10.86%, respectively. Moreover, DMBIM functionalization slightly increased the sensing response of ZIF-67/MXene. The heterostructure of the MOF on the MXene hybrid had excellent charge transfer capacity through a Schottky junction and provided high sensing performances. H-MOF<sub>6</sub>/MXene sensors exhibited rapid response and recovery (25 and 192 s) to 1 ppm of NH<sub>3</sub> at RT

(Fig. S12†), and the H-MOF<sub>6</sub>/MXene sensor had a high recovery rate compared to layered MXene. The mass ratio of the MOF on MXenes crucially influenced the sensing ability of hybrid sensors. Fig. 3b shows the sensing abilities of ZIF-67/MXene with different surface mass loadings of the MOF. Surface conductivity significantly changed as a function of MOF tagging. Increasing the mass loading of ZIF-67 (6 wt%) in the H-MOF<sub>x</sub>/MXene hybrid increased sensor response. However, further increasing the ZIF-67 loading reduced the conductivity and resulted in poor sensing performance.

Fig. 3c shows the electrical resistance of the sensing materials when exposed to NH<sub>3</sub> at different times. The resistance of the pristine MXene nanosheets increased, probably due to carrier reduction after NH<sub>3</sub> adsorption and the effect of this on conductivity.<sup>42</sup> However, the resistance of MOF/MXene decreased, revealing n-type semiconductor behavior.<sup>43</sup> The interaction between NH<sub>3</sub> and oxygen functionalities on the heterostructure surface increased the carrier concentration on ZIF-67/MXene and reduced sensor resistance. The MOF network on MXenes can act as a bridge for carrier transfer that increases the internal redox reaction rate and enhances gas-sensing ability. The dynamic response (Fig. 3d) of the H-MOF<sub>6</sub>/MXene hybrid was more sensitive to NH<sub>3</sub>, and its limit of detection (LOD) was lower than that of MXenes due to a greater number of adsorption sites on the heterostructure surface. MOF/MXene provided a robust, stable response even at low NH<sub>3</sub> concentration (200 ppb) (Fig. 3e). In particular, H-MOF<sub>6</sub>/MXene exhibited a highly stable response to NH<sub>3</sub> with good sensitivity and excellent linearity from 800 ppb to 50 ppm (Fig. 3f). The LODs of H-MOF<sub>6</sub>/MXene and MXene sensors were 12.8 and 59.4 ppb, respectively. Selective adsorption of NH<sub>3</sub> through surface ZIF-67 enhanced selectivity due to an electronic interaction within the zeolite functionality.<sup>44</sup> A comparison of sensing response and durability over five consecutive cycles showed that the H-MOF<sub>6</sub>/MXene sensor produced a strong, durable response (Fig. 3g) to 20 ppm NH<sub>3</sub>, which would be helpful for long-term applications. To study the stability of this sensor, an aging test of the MXene-based sensors was performed over 8 weeks at a relative humidity of 51% at room temperature. Response to 10 ppm NH<sub>3</sub> was reduced by only 5.2%, which showcased excellent long-term stability (Fig. 3h). Response reductions are mainly due to surface oxidization of the MXene and result in increased conductivity. Increasing the DMBIM concentration by increasing diffusion time did not appreciably influence the sensing response (Fig. S13†). Due to the molecular sieve effect, DMDIM is too large to pass through ZIF-67, and hence ligand exchange only occurred on the outermost surface of ZIF-67.<sup>35</sup> Fig. 3i shows the temperature response and temperature resistance of MXene, MOF<sub>6</sub>/MXene, and H-MOF<sub>6</sub>/MXene sensors for 20 ppm NH<sub>3</sub> within the temperature range from 20 °C to 70 °C. While increasing temperature, the resistance of the sensor decreases owing to thermal excitation, which further decreases the response value. Near room temperature, the sensors exhibited high response. On increasing the substrate temperature, the sensing response was reduced due to the poor adsorption of NH<sub>3</sub> on the MXene-based sensing surface. The resistance of the MOF/MXene is increased on modifying H-



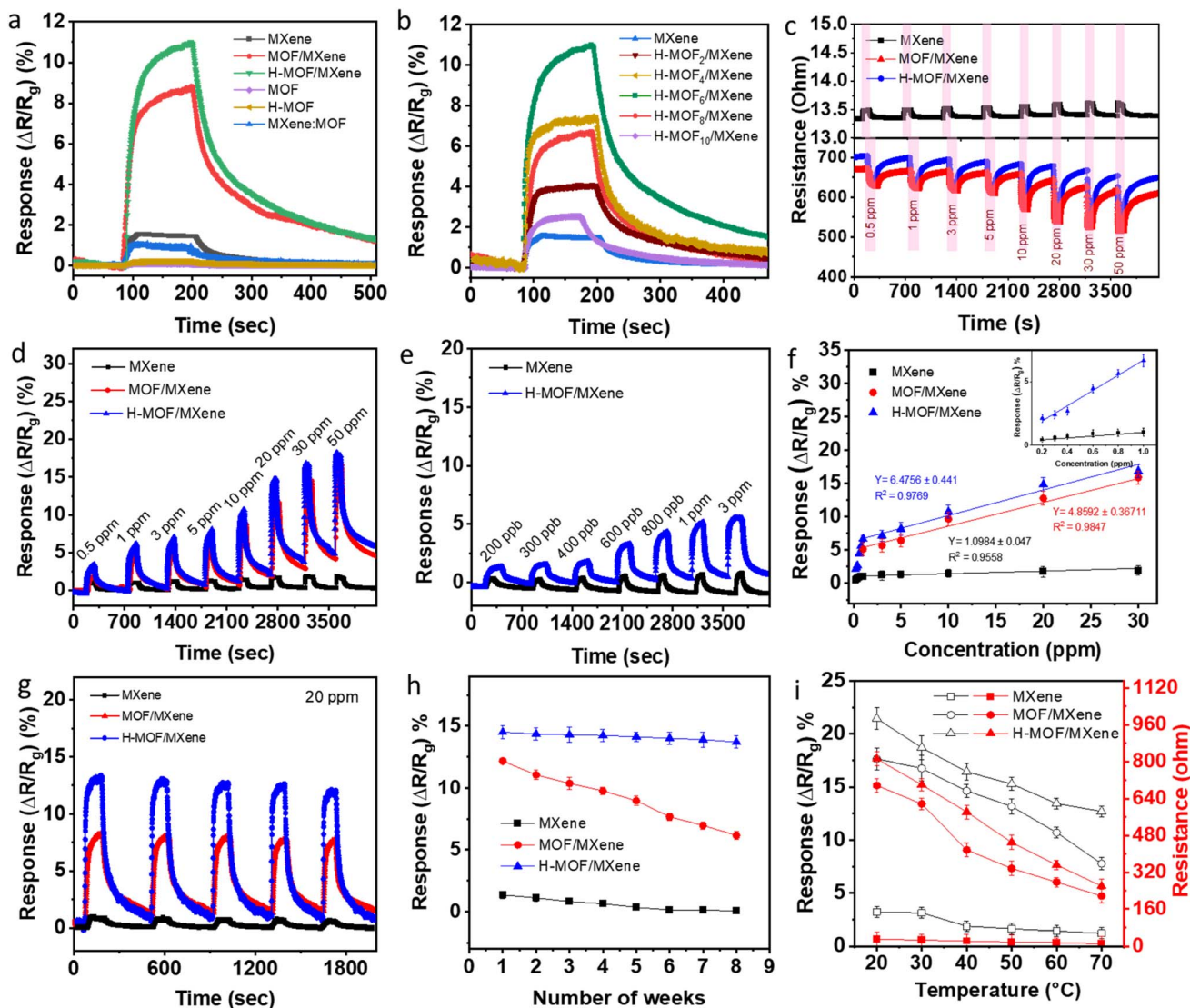


Fig. 3 (a) Typical response of MXenes, ZIF-67, MOF<sub>6</sub>/MXene, H-MOF<sub>6</sub>/MXene, and physically mixed MXene/H-ZIF-67 (1:1) composites to 10 ppm of  $\text{NH}_3$ . (b) The sensing response of H-MOF/MXene with different MOF<sub>x</sub>/MXene mass ratios (x = 2, 4, 6, 8, and 10 wt%). (c) Dynamic resistance, (d and e) dynamic response, and (f) fitting curves of the responses of the MOF on MXene hybrids to  $\text{NH}_3$  concentrations ranging from 200 ppb to 50 ppm at RT (298 K). (g) Repeatability of the MOF on MXene hybrids after 5 cycles of exposure to 20 ppm of  $\text{NH}_3$  at RT. (h) Long-term stability of the MOF on MXene hybrids at RT. (i) Response and resistance of the H-MOF<sub>6</sub>/MXene sensor to 20 ppm of  $\text{NH}_3$  at different temperatures (20–70 °C).

MOF<sub>6</sub>/MXene sensors, which may be due to the surface functionalization that decreases the contact interface and impedes the electron transportation between MXene nanosheets. With respect to the temperature, H-MOF<sub>6</sub>/MXene exhibited a higher response compared to MOF<sub>6</sub>/MXene, which may be due to the broadened depletion layer created on H-MOF<sub>6</sub>/MXene that increases the ability of MXenes to accept free electrons from  $\text{NH}_3$ .

Humidity presents a serious challenge because the adsorption of water molecules on active surface layers, especially on hydrophilic surfaces like MXenes, directly affects sensor responses. However, a hydrophobic active sensing surface effectively minimizes water interference (Fig. 4a). Fig. 4b and c show the typical dynamic gas sensing responses of the MOF<sub>6</sub>/MXene and H-

MOF<sub>6</sub>/MXene sensors at different  $\text{NH}_3$  concentrations and RH values (10, 36, 51, 76, and 93%) to 10 ppm  $\text{NH}_3$ . Notably, the current responses of MOF<sub>6</sub>/MXene and H-MOF<sub>6</sub>/MXene sensors were good in a broad range of  $\text{NH}_3$  concentrations (1–50 ppm). Notably, the MOF<sub>6</sub>/MXene sensor response increased with RH (increases of 1.45% and 1.33% versus response at RH values of 76% and 93%, respectively). This was likely due to competition between  $\text{NH}_3$  and  $\text{H}_2\text{O}$  molecules for adsorption on the sensor surface. On the other hand, H-MOF<sub>6</sub>/MXene sensors exhibited selectivity for  $\text{NH}_3$  with RH tolerance. H-MOF<sub>6</sub>/MXene showed changes of 0.22% at 72% and 0.27% at 93% versus an RH of 10%. The selectivity coefficient ( $\text{SC}_{\text{RH}}$ ) of MOF<sub>6</sub>/MXene was 1.08 at 51% RH, while that of H-MOF<sub>6</sub>/MXene was 0.998 at the same RH. The contact angles of MXenes, MOF<sub>6</sub>/MXene, and H-MOF<sub>6</sub>/MXene



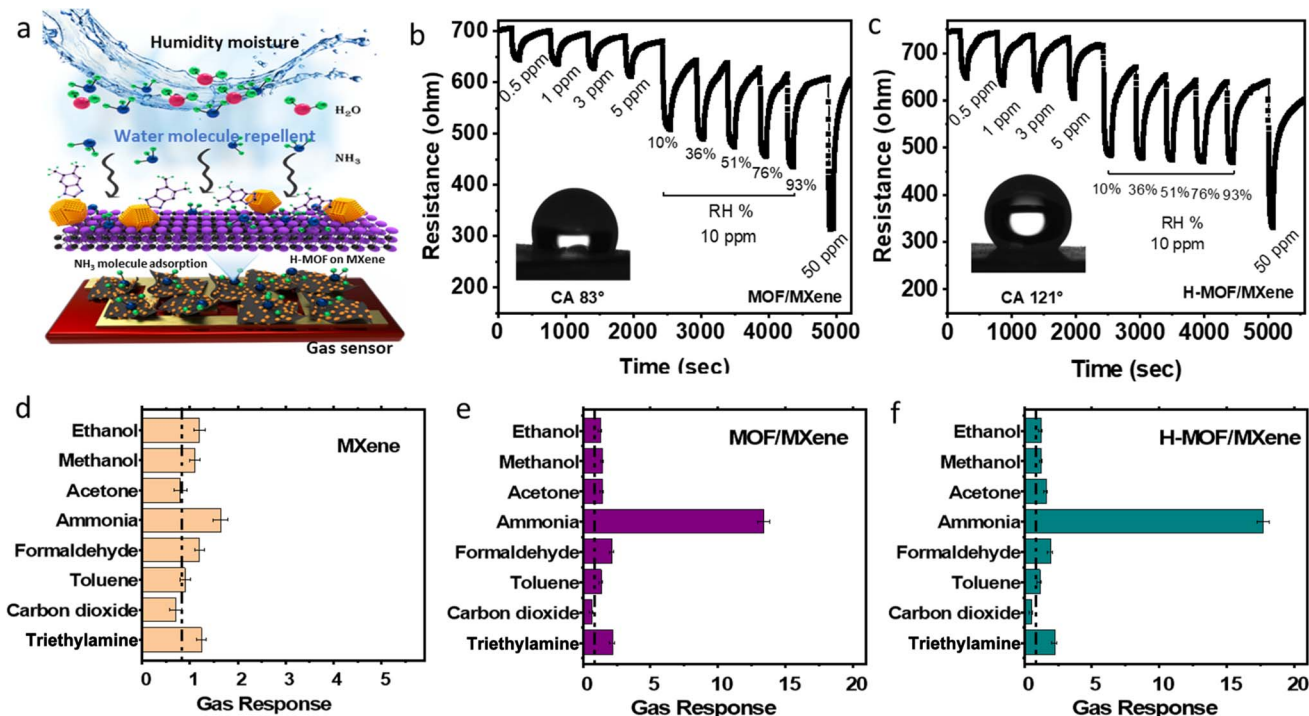


Fig. 4 (a) Schematic illustration of gas sensing in the presence of humidity. The dynamic response/recovery curves of (b) MOF<sub>6</sub>/MXene and (c) H-MOF<sub>6</sub>/MXene sensors upon exposure to different concentrations of NH<sub>3</sub> at different RH levels. (d–f) Selectivities of MXenes, MOF<sub>6</sub>/MXene, and H-MOF<sub>6</sub>/MXene towards various gases (20 ppm) under the same conditions (25 °C). Sensing responses were tested three times. The results are presented as mean response values and error bars represent SDs.

were measured to be 61°, 83°, and 121°, respectively (Fig. 4b, c and S14†). The large contact angle of H-MOF<sub>6</sub>/MXene was attributed to low surface energy due to its hydrophobic nature. Thus, the passive layer of DMDIM on MOF<sub>6</sub>/MXene reduced surface affinity for water and protected the layered sensing surface from humidity. The responses of MOF<sub>6</sub>/MXene and H-MOF<sub>6</sub>/MXene sensors were also tested at different RH values in the absence of NH<sub>3</sub> (Fig. S15†). While the responses of the MOF<sub>6</sub>/MXene sensor increased with humidity, the H-MOF<sub>6</sub>/MXene sensor exhibited only a minimal increase when varying the RH% to address the anti-humidity performance of the sensor. For the H-MOF<sub>6</sub>/MXene sensors, DMDIM functionality acts as a shield that minimizes the adsorption of water molecules on the sensing surface due to the hydrophobic nature. Therefore, water molecules cannot react with chemisorbed oxygen ions (O<sup>−</sup>) and induce free electrons, so the response for the H-MOF<sub>6</sub>/MXene sensor at different humidity levels remains almost the same.

Designing the MOF on MXene heterostructure assembly provided a high sensitivity and selectivity towards NH<sub>3</sub>. The selectivity of the different sensors is presented in Fig. 4d–f in the presence of different volatile organics. The MXene surface responded to most analytes (Fig. 4d), whereas MOF<sub>6</sub>/MXene exhibited better selectivity for NH<sub>3</sub> with a higher response ( $R_a/R_g = 13.37$ , 10 ppm) than acetone ( $R_a/R_g = 1.41$ , 10 ppm), ethanol ( $R_a/R_g = 1.24$ , 10 ppm), methanol ( $R_a/R_g = 1.45$ , 10 ppm), formaldehyde ( $R_a/R_g = 2.12$ , 10 ppm), CO<sub>2</sub> ( $R_a/R_g = 0.61$ , 10 ppm), triethylamine ( $R_a/R_g = 2.14$ , 10 ppm), and toluene ( $R_a/R_g = 1.36$ , 10 ppm). This selectivity for NH<sub>3</sub> was due to the selective adsorption of NH<sub>3</sub> on

the ZIF-67 surface and the Schottky junction between the ZIF-67 and MXene, which promoted effective carrier transportation. H-MOF<sub>6</sub>/MXene had an NH<sub>3</sub> sensing response nearly 8 times greater than those of VOCs (Fig. 4f), and this response was better than those in previous reports.<sup>19,25</sup> The conductivity of the MXene and the high absorption characteristics of ZIF-67 increased the charge carrier transfer rate on MOF<sub>6</sub>/MXene, indicating a gas sensing mechanism involving a Schottky junction. Thus, the structural defects endowed by the MOF on MXenes, sufficient active sites, and a p–n multi-phase heterointerface increased electron transport capacity. To further address the superiority of the MOF/MXene sensor, Table 1 summarizes and compares the gas sensing response with that of other reported MXene-based sensors. The designed MOF/MXene sensor demonstrates high sensitivity and offers the advantages of low pLOD and response/recovery time.

The *I–V* characteristics of MXene hybrids were investigated to obtain insights into sensitivities, contact interfaces, and mechanisms. Sensors were fabricated on Au interdigitated electrodes, and total sensor resistances were expressed as  $R_{\text{total}}$  ( $R_{\text{total}} = R_{\text{material}} + R_{\text{contact}} + R_{\text{electrodes}}$ ). The *I–V* characteristics of MXenes on the Au electrode exhibited a symmetrical linear characteristic representing an ohmic contact (Fig. 5a). On the other hand, the MOF on the Au electrode had poor electrical response due to its low conductivity at RT. On the other hand, the *I–V* curve of MOF<sub>6</sub>/MXene on the Au electrode surface indicated a symmetrical Schottky contact interface, and that of H-MOF<sub>6</sub>/MXene a symmetrical contact with non-rectifying



Table 1 Comparison of MXene hybrid chemiresistive sensors at room temperature

Material	Gas	Gas concentration	Response	$T_{\text{res}}/T_{\text{rec}}$ (s)	pLOD	Ref.
H-MOF <sub>6</sub> /MXene	NH <sub>3</sub>	10 ppm	13.37 <sup>a</sup>	25/192	12.8 ppb	This work
Co-TCPP(Fe)/Ti <sub>3</sub> C <sub>2</sub> T <sub>x</sub>	NO	10 ppm	2.2 <sup>b</sup>	95/15	200 ppb	19
Ti <sub>3</sub> C <sub>2</sub> T <sub>x</sub> -PVDF-ZIF-67	NH <sub>3</sub>	25 ppm	10.56 <sup>a</sup>	41/75	1 ppb	25
MXene/In <sub>2</sub> O <sub>3</sub>	NH <sub>3</sub>	20 ppm	100.7 <sup>a</sup>	60/300	1000 ppb	45
MXene/graphene	NH <sub>3</sub>	100 ppm	25.0 <sup>a</sup>	26/148	56 ppb	46
MXene/SnO <sub>2</sub>	NH <sub>3</sub>	50 ppm	40 <sup>a</sup>	36/44	4.29 ppb	47
Ti <sub>3</sub> C <sub>2</sub> T <sub>x</sub> /TiO <sub>2</sub>	NH <sub>3</sub>	10 ppm	3.1 <sup>a</sup>	60/750	500 ppb	48
Ti <sub>3</sub> C <sub>2</sub> T <sub>x</sub> /WSe <sub>2</sub>	Ethanol	40 ppm	9.2 <sup>a</sup>	9.7/6.6	—	49
MoS <sub>2</sub> /Ti <sub>3</sub> C <sub>2</sub> T <sub>x</sub>	NO <sub>2</sub>	20 ppm	40.1 <sup>a</sup>	525/155	—	50
Ti <sub>3</sub> C <sub>2</sub> T <sub>x</sub> -TiO <sub>2</sub>	Hexanal	10 ppm	~3.4 <sup>b</sup>	293/461	10 ppm	51
$\alpha$ -Fe <sub>2</sub> O <sub>3</sub> /Ti <sub>3</sub> C <sub>2</sub> T <sub>x</sub>	Acetone	5 ppm	16.6 <sup>a</sup>	5/5	0.56 ppm	52
CoPM-24	NO <sub>x</sub>	100 ppm	27.9 <sup>b</sup>	2/73	30 ppb	53
MXene@TiO <sub>2</sub> /MoS <sub>2</sub>	NH <sub>3</sub>	100 ppm	163.3 <sup>a</sup>	117/88	—	54
MXene/WS <sub>2</sub>	NO <sub>2</sub>	2 ppm	17.4 <sup>a</sup>	407/336	10 ppb	55
In <sub>2</sub> O <sub>3</sub> /ZnO/MXene	Ethanol	100 ppm	6.5 <sup>b</sup>	48/116	—	56
2H-MoS <sub>2</sub> /Ti <sub>3</sub> C <sub>2</sub> T <sub>x</sub>	NO <sub>2</sub>	100 ppm	65.6 <sup>a</sup>	6.2/5.1	1.15 ppm	57
CuO/Ti <sub>3</sub> C <sub>2</sub> T <sub>x</sub>	NO <sub>2</sub>	100 ppm	38.54 <sup>a</sup>	2.1/32.4	0.003 ppm	58
CPAM/Ti <sub>3</sub> C <sub>2</sub> T <sub>x</sub>	NH <sub>3</sub>	150 ppm	3.1 <sup>b</sup>	12.7/14.6	—	59
SnO/SnO <sub>2</sub> /Ti <sub>3</sub> C <sub>2</sub> T <sub>x</sub>	Acetone	100 ppm	12.1 <sup>b</sup>	18/9	—	60

<sup>a</sup>  $S = (R_a - R_g)/R_a \times 100\%$  or  $S = (R_g - R_a)/R_g \times 100\%$ . <sup>b</sup>  $S = R_a/R_g$ .

behavior. The reverse current was slightly less than the forward current for H-MOF<sub>6</sub>/MXene. Additionally, XPS analysis of the O 1s spectra of H-MOF<sub>6</sub>/MXene (Fig. 5b) reveals that after the adsorption of NH<sub>3</sub>, the ratio of surface chemisorbed oxygen/surface hydroxyl groups on H-MOF<sub>6</sub>/MXene was reduced to 27%, demonstrating the chemical interaction of ammonia on the sensing surface promoting electron transfer. The peak shifted towards the right by 0.4 eV after NH<sub>3</sub> adsorption evidencing the metal-hydroxyl formation on the sensing surface.<sup>61</sup> This result shows that surface-adsorbed O functionalities also participate in sensing. Furthermore, the shift shown by Co 2p to higher binding energy after exposure to NH<sub>3</sub> resulted in charge transfer between MOF/MXene and adsorbed NH<sub>3</sub> (Fig. S16†). The FTIR spectrum of H-MOF<sub>6</sub>/MXene after NH<sub>3</sub> adsorption (Fig. 5c) showed N-H stretch at 648, 1356, and 3335 cm<sup>-1</sup>, which resulted in NH<sub>3</sub>-related products being adsorbed on H-MOF<sub>6</sub>/MXene as NH<sub>3</sub><sup>+</sup>. On introducing ZIF-67 on the MXene surface, the selectivity for NH<sub>3</sub> has been promoted through the selective adsorption properties towards the NH<sub>3</sub> gases.<sup>62</sup> The selective pore size and acid-base interaction within the zeolite groups induce the selectivity towards NH<sub>3</sub>.<sup>25</sup> Meanwhile, MXenes have high sensitivity towards NH<sub>3</sub> through -OH, and -O based surface functionalities due to their high adoption energy as compared with that of other analytes such as CO<sub>2</sub>, NO<sub>2</sub>, CH<sub>4</sub>, and CO.<sup>63</sup> On the other hand, a building block of MOF on MXenes as a hybrid interface induced selectivity by blocking specific pores, enabling only the selectivity towards NH<sub>3</sub>, which minimizes the interaction of other gases and VOCs. The loading density of the MOF on MXenes plays a crucial role in the conductivity of MXenes that impacts the sensitive response of the hybrid surface. Furthermore, the rapid desorption of NH<sub>3</sub> from the hybrid surface would aid sensor recovery (Fig. S17†). The work functions of MXenes and the MOF were obtained from previous reports,<sup>19,64</sup> and the band gap

was calculated using UV-DRS absorption spectra and a K-M plot (Fig. S18†). Band gaps for MXenes, ZIF-67, MOF<sub>6</sub>/MXene, and the H-MOF<sub>6</sub>/MXene hybrid were 1.61, 1.96, 1.86, and 1.90 eV, respectively. Band gaps are crucial parameters because narrow band gaps favor charge transfer. The highest occupied molecular orbital (HOMO) and the lowest occupied molecular orbital (LOMO) of ZIF-67-MXene before and after assembly are provided in Fig. 5d. The  $E_f$  of MXenes was close to the HOMO which is represented by the p-type semiconductor behavior. The ZIF-67/MXene heterostructure exhibited the n-type semiconductor behavior which shows that the  $E_f$  will be close to the LOMO.

According to predicted work functions, an external bias voltage causes electrons to migrate from the MOF to MXenes, which is favored by Schottky junction formation and in line with our XPS results. After forming the heterostructure, the  $E_f$  of MOF/MXene was close to the MOF LOMO level, resulting from n-type semiconductive behavior which has been confirmed through the Mott-Schottky plot of the H-MXene/MXene heterostructure (Fig. S19†). The electrochemical characteristics of the charge transfer capabilities of the MXene, MOF, and MOF<sub>6</sub>/MXene hybrid were analyzed (Fig. S20†). The equivalent circuit diagram of the H-MOF<sub>6</sub>/MXene electrode was provided with the respective specific impedance values. H-MOF<sub>6</sub>/MXene had the smallest Nyquist circle next to the MXene with low internal charge transfer resistance and improved charge carrier transportation efficiency. The internal charge transfer resistance of H-MOF<sub>6</sub>/MXene was lower than that of the MOF, which showed that the Schottky interface of MXenes promotes charge transfer efficiency. In addition, MOF integrity on MXenes would lead to favorable energy band positions and a Fermi level that reduces the electrical conductivity of Ti<sub>3</sub>T<sub>2</sub>T<sub>x</sub> MXene. The NH<sub>3</sub> sensing mechanism of the MOF on MXenes is shown in Fig. 5e. The H-MOF<sub>6</sub>/MXene heterostructure exhibited intimate contact



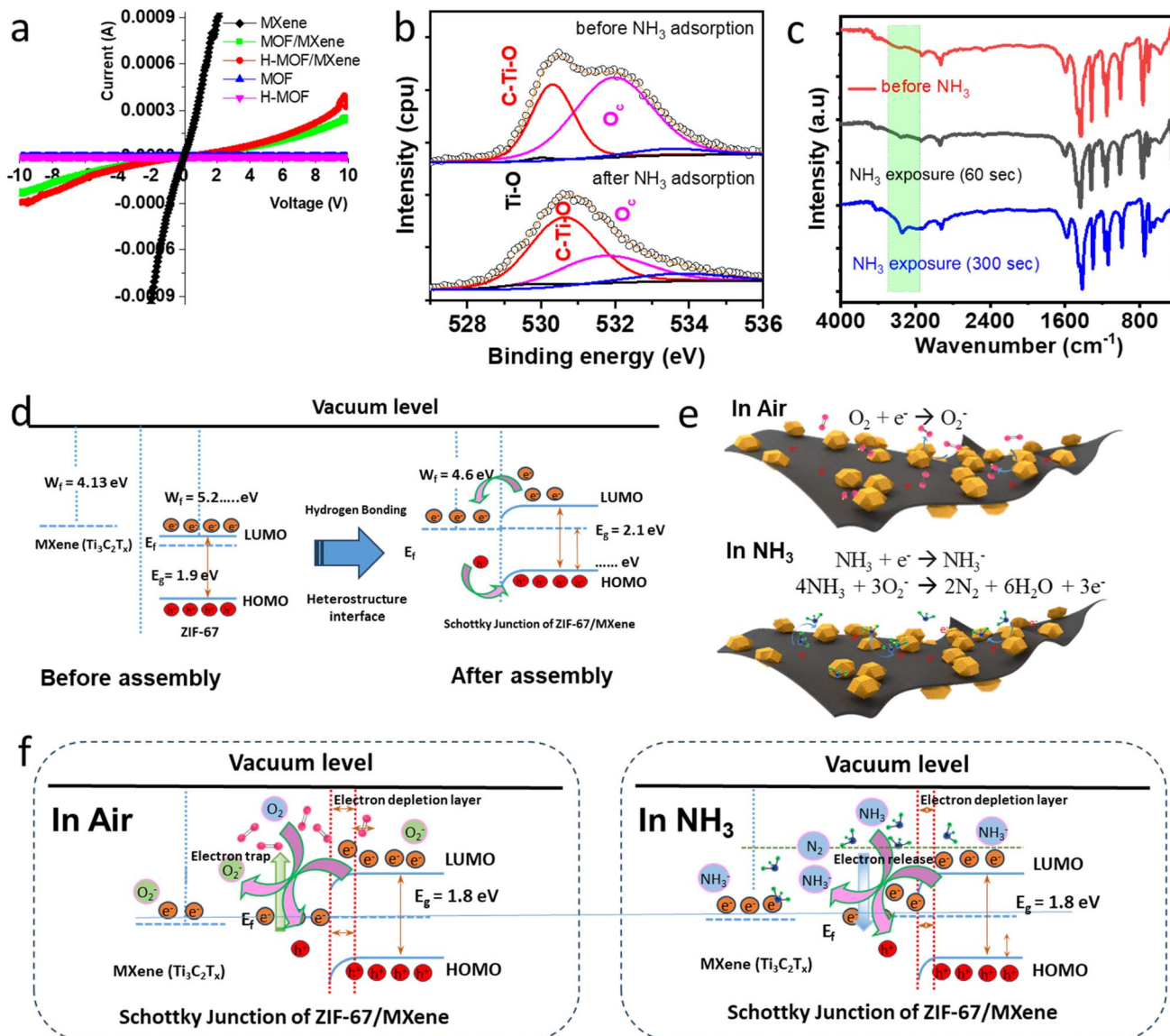


Fig. 5 (a) *I*–*V* characteristics of the different MXene hybrids. (b) O 1s XPS spectra and (c) FTIR spectra of H-MOF<sub>6</sub>/MXene in air and after exposure to NH<sub>3</sub> at RT. (d) Energy schemes of MXenes and the MOF on MXenes before and after heterostructure assembly. (e) Schematic of the gas sensing mechanism of the H-MOF<sub>6</sub>/MXene heterostructure. (f) Energy band diagram of the H-MOF<sub>6</sub>/MXene heterostructure in air and after NH<sub>3</sub> interaction on the sensing surface.

between H-ZIF-67 and MXenes due to hydrogen bond formation. The heterostructure interface created a Schottky junction with a narrow band function, and the  $E_f$  of ZIF-67 in the vicinity of MXenes enabled charge transfer from the MOF/MXene surface to NH<sub>3</sub>. The diffusion coefficient of the analyte also plays a significant role in the hybrid surface. Loading the MOF on MXenes created many active porous features, which allowed analytes to flow through the rough features of the layered surface. The diffusion coefficient is inversely related to the square root of the molecular weight ( $\text{g g}^{-1} \text{mol}^{-1}$ ) of the target gas. Among the gases examined, NH<sub>3</sub> ( $\sim 17.03$ ) is the lightest, followed by methanol ( $\sim 32.04$ ), CO<sub>2</sub> ( $\sim 44.01$ ), ethanol ( $\sim 46.07$ ), and acetone ( $\sim 58.08$ ), which resulted in the high possible interaction of NH<sub>3</sub> on the sensing surface.<sup>25</sup> Furthermore, when

the H-MOF/MXene sensor was exposed to air, O<sub>2</sub> molecules captured electrons and converted them into chemisorbed O<sub>2</sub><sup>-</sup> species at the heterostructure interface, and when such sensors were exposed to NH<sub>3</sub>, target gases interacted with species, such as OH and -O, and captured electrons from the MOF to form NH<sub>3</sub><sup>-</sup> (NH<sub>3</sub> + e<sup>-</sup> → NH<sub>3</sub><sup>-</sup>). As a result, the MOF has reduced the resistance of the MXene surface, which generated gas-sensing signals. The surface-tagged MOF on MXenes would prevent aggregation and maximize gas adsorption, which, in turn, would maximize free electron density on the sensor surface. Furthermore, the adsorption of chemisorbed oxygen would enhance the electron-depleted layer and the potential barrier at the contact interface. The creation of a space charge region at the interface would maximize the generation of adsorbed





oxygen ions on the surface and increase sensor resistance. On the other hand, less interaction with  $\text{NH}_3$  would release more electrons, reduce the width of the electron depletion layer, increase the conductivity of the MOF/MXene heterostructure, and thus, improve sensitivity for  $\text{NH}_3$  detection. In addition, our observations showed that excessive amounts of MOF on MXenes destroy the Schottky junction. The rapid carrier response of the MOF underlies its reversible response, and MXenes play a supportive role as a conductive layer that contributes to gas sensing performance. The work function is a significant parameter for constructing high-performance heterostructured sensing materials with high sensitivity and selectivity.

## 4 Conclusion

In summary, intimate contact between the MOF and a layered MXene heterostructure and capping with DMBIM using the SLAR process were achieved by impregnating Co ions on the MXene as a template for the interaction with ZIF-67. A comprehensive study was conducted to investigate the impact of DMBIM capping on MOF/MXene surfaces. The surface modification and improved hydrophobicity on the DMBIM-capped MOF surface were analyzed using contact angle, FTIR, Raman, and XPS measurements. The Schottky junction-based interface featuring hydrogen bonds maximized charge transportation across the interface and played a crucial role in RT  $\text{NH}_3$  sensing performance. DMBIM capping facilitated excellent gas sensing performance for  $\text{NH}_3$  ( $R_a/R_g = 6.9$ , 1 ppm) with a theoretical LOD of 12.8 ppb, reliable repeatability (>five times), and durability >8 weeks. Furthermore, MOF-tagged MXenes showed outstanding selectivity for  $\text{NH}_3$  and the surface modification of DMBIM created hydrophobicity (water contact angle of  $121^\circ$ ) that protects the adsorption of water molecules on the sensing surface and creates anti-humidity properties. The humidity tolerance of the DMBIM-capped MOF on MXenes has a negligible response towards the different RH%, and the sensing response was  $\sim 8$  times that of MXene sensors. The facile constructions of the MOF on MXenes with a Schottky junction for high-performance, humidity-tolerant chemiresistive sensors that function at RT, would guide the design of MOF-based hybrid sensing materials for future applications.

## Data availability

The data supporting this article have been included as part of the ESI.†

## Conflicts of interest

The authors declare no competing financial interest.

## Acknowledgements

This work was supported by the National Research Foundation of Korea (NRF) grant funded by the Korean Government (MSIT)

(2022R1C1C1010601 and 2022R1A2C2008968). This work was also financially supported by "Cooperative Research Program for Agriculture Science and Technology Development (Project No. PJ01706703)" Rural Development Administration, Republic of Korea.

## References

- 1 K. Kim, A. Zagalskaya, J. L. Ng, J. Hong, V. Alexandrov, T. A. Pham and X. Su, Coupling nitrate capture with ammonia production through bifunctional redox-electrodes, *Nat. Commun.*, 2023, **14**, 823, DOI: [10.1038/s41467-023-36318-1](https://doi.org/10.1038/s41467-023-36318-1).
- 2 J. Kong, H. Kim and H. S. Park, Electrochemical  $\text{NH}_3$  production: *In-situ* evaluation of the activity and durability of nitrogen-reduction catalysis using scanning electrochemical microscopy (SECM), *Appl. Catal., B*, 2023, **338**, 123019, DOI: [10.1016/j.apcatb.2023.123019](https://doi.org/10.1016/j.apcatb.2023.123019).
- 3 B. Yang, X. Li, Z. Hua, Z. Li, X. He, R. Yan, Y. Li, Z. Zhi and C. Tian, A low cost and high performance  $\text{NH}_3$  detection system for a harsh agricultural environment, *Sens. Actuators, B*, 2022, **361**, 131675, DOI: [10.1016/j.snb.2022.131675](https://doi.org/10.1016/j.snb.2022.131675).
- 4 R. Paul, B. Das and R. Ghosh, Novel approaches towards design of metal oxide based hetero-structures for room temperature gas sensor and its sensing mechanism: A recent progress, *J. Alloys Compd.*, 2023, **941**, 168943, DOI: [10.1016/j.jallcom.2023.168943](https://doi.org/10.1016/j.jallcom.2023.168943).
- 5 A. Singh, S. Sikarwar, A. Verma and B. C. Yadav, The recent development of metal oxide heterostructures based gas sensor, their future opportunities and challenges: A review, *Sens. Actuators, A*, 2021, **332**, 113127, DOI: [10.1016/j.sna.2021.113127](https://doi.org/10.1016/j.sna.2021.113127).
- 6 L. Liu, Y. Wang, Y. Liu, S. Wang, T. Li, S. Feng, S. Qin and T. Zhang, Heteronanostructural metal oxide-based gas microsensors, *Microsyst. Nanoeng.*, 2022, **8**, 85, DOI: [10.1038/s41378-022-00410-1](https://doi.org/10.1038/s41378-022-00410-1).
- 7 X. Chen, T. Liu and X. T. Yin, High response triethylamine gas sensor based on flaky W-doped  $\text{MoO}_3$ , *J. Ind. Eng. Chem.*, 2024, **129**, 691–698, DOI: [10.1016/j.jiec.2023.09.027](https://doi.org/10.1016/j.jiec.2023.09.027).
- 8 Z. Wang, M. Bu, N. Hu and L. Zhao, An overview on room-temperature chemiresistor gas sensors based on 2D materials: Research status and challenge, *Composites, Part B*, 2023, **248**, 110378, DOI: [10.1016/j.compositesb.2022.110378](https://doi.org/10.1016/j.compositesb.2022.110378).
- 9 Y. Xiao, H. Li, C. Wang, S. Pan, J. He, A. Liu, J. Wang, P. Sun, F. Liu and G. Lu, Room Temperature Wearable Gas Sensors for Fabrication and Applications, *Adv. Sens. Res.*, 2024, **3**, 2300035, DOI: [10.1002/adsr.202300035](https://doi.org/10.1002/adsr.202300035).
- 10 Y. Cheng, B. Ren, K. Xu, I. Jeerapan, H. Chen, Z. Li and J. Z. Ou, Recent progress in intrinsic and stimulated room-temperature gas sensors enabled by low-dimensional materials, *J. Mater. Chem. C*, 2021, **9**, 3026–3051, DOI: [10.1039/D0TC04196C](https://doi.org/10.1039/D0TC04196C).
- 11 Y. Zhao, J. Zhang, X. Guo, X. Cao, S. Wang, H. Liu and G. Wang, Engineering strategies and active site identification of MXene-based catalysts for electrochemical



- conversion reactions, *Chem. Soc. Rev.*, 2023, **52**, 3215–3264, DOI: [10.1039/D2CS00698G](#).
- 12 N. K. Chourasia, A. Rawat, R. K. Chourasia, H. Singh, R. K. Kulriya, V. Singh and P. K. Kulriya, Unveiling the potential of  $\text{Ti}_3\text{C}_2\text{T}_x$  MXene for gas sensing: recent developments and future perspectives, *Materials Advances*, 2023, **4**, 5948–5973, DOI: [10.1039/D3MA00631J](#).
  - 13 R. Bhardwaj and A. Hazra, MXene-based gas sensors, *J. Mater. Chem. C*, 2021, **9**, 15735–15754, DOI: [10.1039/D1TC04085E](#).
  - 14 Y. Han, H. Cao, Y. Cao, X. Wen, Y. Yao and Z. Zhu, Fast response flexible humidity sensors based on  $\text{Ti}_3\text{C}_2\text{T}_x$  MXene-heterostructures for multifunctional applications, *J. Mater. Chem. C*, 2024, **12**, 4809–4816, DOI: [10.1039/D4TC00111G](#).
  - 15 F. Cao, Y. Zhang, H. Wang, K. Khan, A. K. Tareen, W. Qian, H. Zhang and H. Agren, Recent Advances in Oxidation Stable Chemistry of 2D MXenes, *Adv. Mater.*, 2022, **34**, 2107554, DOI: [10.1002/adma.202107554](#).
  - 16 S. J. Kim, H.-J. Koh, C. E. Ren, O. Kwon, K. Maleski, S.-Y. Cho, B. Anasori, C.-K. Kim, Y.-K. Choi, J. Kim, Y. Gogotsi and H.-T. Jung, Metallic  $\text{Ti}_3\text{C}_2\text{T}_x$  MXene Gas Sensors with Ultrahigh Signal-to-Noise Ratio, *ACS Nano*, 2018, **12**, 986–993, DOI: [10.1021/acsnano.7b07460](#).
  - 17 S. Kim, T. Y. Ko, A. K. Jena, A. S. Nissimagoudar, J. Lee, S. Lee, T. Oh, Y. C. Kang, I. In, S. Bhattacharjee, C. M. Koo, S.-C. Lee and S. J. Kim, Instant Self-Assembly of Functionalized MXenes in Organic Solvents: General Fabrication to High-Performance Chemical Gas Sensors, *Adv. Funct. Mater.*, 2024, **34**, 2310641, DOI: [10.1002/adfm.202310641](#).
  - 18 T. Habib, X. Zhao, S. A. Shah, Y. Chen, W. Sun, H. An, J. L. Lutkenhaus, M. Radovic and M. J. Green, Oxidation stability of  $\text{Ti}_3\text{C}_2\text{T}_x$  MXene nanosheets in solvents and composite films, *npj 2D Mater. Appl.*, 2019, **3**, 8, DOI: [10.1038/s41699-019-0089-3](#).
  - 19 Y. Chang, M. Chen, Z. Fu, R. Lu, Y. Gao, F. Chen, H. Li, N. F. Rooij, Y.-K. Lee, Y. Wang and G. Zhou, Building porphyrin-based MOFs on MXenes for ppb-level NO sensing, *J. Mater. Chem. A*, 2023, **11**, 6966–6977, DOI: [10.1039/D3TA00072A](#).
  - 20 X. Wu, M. Niu, X. Tian, X. Peng, P. J. S. Buenconsej, X. Wu, Y. Wang, W. Ji, Y. Li, J. Qiao, J. Tao, M. Zhang, S. Xiao and H. Yuan, Solution-processable  $\text{Ni}_3(\text{HITP})_2/\text{MXene}$  heterostructures for ppb-level gas detection, *J. Mater. Chem. A*, 2024, **12**, 17382–17394, DOI: [10.1039/D4TA02438A](#).
  - 21 X. Zhao, K. Tao and L. Han, Self-supported metal-organic framework-based nanostructures as binder-free electrodes for supercapacitors, *Nanoscale*, 2022, **14**, 2155–2166, DOI: [10.1039/D1NR08284A](#).
  - 22 N. Garg, A. Deep and A. L. Sharma, Metal-organic frameworks based nanostructure platforms for chemoresistive sensing of gases, *Coord. Chem. Rev.*, 2021, **445**, 214073, DOI: [10.1016/j.ccr.2021.214073](#).
  - 23 W. Yan, H. Xu, M. Ling, S. Zhou, T. Qiu, Y. Deng, Z. Zhao and E. Zhang, MOF-Derived Porous Hollow  $\text{Co}_3\text{O}_4/\text{ZnO}$  Cages for High-Performance MEMS Trimethylamine Sensors, *ACS Sens.*, 2021, **6**, 2613–2621, DOI: [10.1021/acssensors.1c00315](#).
  - 24 Q. Yu, R. Jin, L. Zhao, T. Wang, F. Liu, X. Yan, C. Wang, P. Sun and G. Lu, MOF-Derived Mesoporous and Hierarchical Hollow-Structured  $\text{In}_2\text{O}_3\text{-NiO}$  Composites for Enhanced Triethylamine Sensing, *ACS Sens.*, 2021, **6**, 3451–3461, DOI: [10.1021/acssensors.1c01374](#).
  - 25 N. K. Arkoti and K. Pal, Selective Detection of  $\text{NH}_3$  Gas by  $\text{Ti}_3\text{C}_2\text{T}_x$  Sensors with the PVDF-ZIF-67 Overlayer at Room Temperature, *ACS Sens.*, 2024, **9**, 1465–1474, DOI: [10.1021/acssensors.3c02551](#).
  - 26 S. Zhang, Y. Ding, Q. Wang and P. Song, MOFs-derived  $\text{In}_2\text{O}_3/\text{ZnO}/\text{Ti}_3\text{C}_2\text{T}_x$  MXene ternary nanocomposites for ethanol gas sensing at room temperature, *Sens. Actuators, B*, 2023, **393**, 134122, DOI: [10.1016/j.snb.2023.134122](#).
  - 27 H. Wang, R. Zhao, J. Qin, H. Hu, X. Fan, X. Cao and D. Wang, MIL-100(Fe)/ $\text{Ti}_3\text{C}_2$  MXene as a Schottky Catalyst with Enhanced Photocatalytic Oxidation for Nitrogen Fixation Activities, *ACS Appl. Mater. Interfaces*, 2019, **11**, 44249–44262, DOI: [10.1021/acsami.9b14793](#).
  - 28 Y. Ji, Y. You, G. Xu, X. Yang and Y. Liu, Engineering metal-organic framework (MOF)@MXene based electrodes for hybrid supercapacitors – A review, *Chem. Eng. J.*, 2024, **483**, 149365, DOI: [10.1016/j.cej.2024.149365](#).
  - 29 Y. An, X. Lv, W. Jiang, L. Wang, Y. Shi, X. Hang and H. Pang, The stability of MOFs in aqueous solutions-research progress and prospects, *Green Chemical Engineering*, 2024, **5**, 187–204, DOI: [10.1016/j.gce.2023.07.004](#).
  - 30 L.-H. Xie, M.-M. Xu, X.-M. Liu, M.-J. Zhao and J.-R. Li, Hydrophobic Metal-Organic Frameworks: Assessment, Construction, and Diverse Applications, *Adv. Sci.*, 2020, **7**, 1901758, DOI: [10.1002/advs.201901758](#).
  - 31 Y. Liang, X. Yang, X. Wang, Z.-J. Guan, H. Xing and Y. Fang, A cage-on-MOF strategy to coordinatively functionalize mesoporous MOFs for manipulating selectivity in adsorption and catalysis, *Nat. Commun.*, 2023, **14**, 5223, DOI: [10.1038/s41467-023-40973-9](#).
  - 32 M. Wen, Y. Xing, G. Liu, S. Hou and S. Hou, Electrochemical sensor based on  $\text{Ti}_3\text{C}_2$  membrane doped with UIO-66- $\text{NH}_2$  for dopamine, *Microchim. Acta*, 2022, **189**, 141, DOI: [10.1007/s00604-022-05222-8](#).
  - 33 X. Liang, Y. Yan, G. Liu, S. Hou and S. Hou, Constructing magnetically functionalized sandwich-like Eu-MOF/PDA@MXene hybrids for extremely sensitive molecular imprinted sensor toward trace detecting trimethylamine oxide, *Chem. Eng. J.*, 2024, **483**, 149301, DOI: [10.1016/j.cej.2024.149301](#).
  - 34 K. S. Ranjith, S.-Y. Lee, S. M. Ghoreishian, N. R. Chodankar, G. S. R. Raju, S. J. Patil, Y. S. Huh, S.-J. Park and Y.-K. Han, Defect and interface engineering of MXene-tagged N, F-doped carbon- $\text{CoSe}_2$  heterostructure for superior hydrogen evolution reactions and supercapacitors, *Carbon*, 2023, **206**, 246–259, DOI: [10.1016/j.carbon.2023.02.021](#).
  - 35 X. Liu, Y. Li, Y. Ban, Y. Peng, H. Jin, H. Bux, L. Xu, J. Caro and W. Yang, Improvement of hydrothermal stability of zeolitic imidazolate frameworks, *Chem. Commun.*, 2013, **49**, 9140–9142, DOI: [10.1039/C3CC45308A](#).



- 36 J. Li, Z. Li, X. Liu, C. Li, Y. Zheng, K. W. K. Yeung, Z. Cui, Y. Liang, S. Zhu, W. Hu, Y. Qi, T. Zhang, X. Wang and S. Wu, Interfacial engineering of  $\text{Bi}_2\text{S}_3/\text{Ti}_3\text{C}_2\text{T}_x$  MXene based on work function for rapid photo-excited bacteria-killing, *Nat. Commun.*, 2021, **12**, 1224, DOI: [10.1038/s41467-021-21435-6](https://doi.org/10.1038/s41467-021-21435-6).
- 37 A. M. Mohamed, M. Ramadan, N. Ahmed, A. O. A. ElNaga, H. H. Alalawy, T. Zaki, S. A. Shaban, H. B. Hassan and N. K. Allam, Metal–Organic frameworks encapsulated with vanadium-substituted heteropoly acid for highly stable asymmetric supercapacitors, *J. Energy Storage*, 2020, **28**, 101292, DOI: [10.1016/j.est.2020.101292](https://doi.org/10.1016/j.est.2020.101292).
- 38 T. Rasheed, A. Rasheed, S. Munir, S. Ajmal, Z. M. Shahzad, I. A. Alsafari, S. A. Ragab, P. O. Agboola and I. Shakir, A cost-effective approach to synthesize  $\text{NiFe}_2\text{O}_4/\text{MXene}$  heterostructures for enhanced photodegradation performance and anti-bacterial activity, *Adv. Powder Technol.*, 2021, **32**, 2248–2257, DOI: [10.1016/j.apt.2021.05.006](https://doi.org/10.1016/j.apt.2021.05.006).
- 39 A. Sengupta, B. V. B. Rao, N. Sharma, S. Parmar, V. Chavan, S. K. Singh, S. Kale and S. Ogale, Comparative evaluation of MAX, MXene, NanoMAX, and NanoMAX-derived-MXene for microwave absorption and Li-ion battery anode applications, *Nanoscale*, 2020, **12**, 8466–8476, DOI: [10.1039/C9NR10980C](https://doi.org/10.1039/C9NR10980C).
- 40 L. Ma, X. Zhang, M. Ikram, M. Ullah, H. Wu and K. Shi, Controllable synthesis of an intercalated ZIF-67/EG structure for the detection of ultratrace  $\text{Cd}^{2+}$ ,  $\text{Cu}^{2+}$ ,  $\text{Hg}^{2+}$  and  $\text{Pb}^{2+}$  ions, *Chem. Eng. J.*, 2020, **395**, 125216, DOI: [10.1016/j.cej.2020.125216](https://doi.org/10.1016/j.cej.2020.125216).
- 41 C. Soosaimanickam, A. Sakthivel, K. Murugavel and S. Alwarappan, Zeolite Imidazolate Framework-Based Platform for the Electrochemical Detection of Epinephrine, *J. Electrochem. Soc.*, 2023, **170**, 107504, DOI: [10.1149/1945-7111/acff21](https://doi.org/10.1149/1945-7111/acff21).
- 42 Z. Kan, F. Shi, L. Yang, Q. Zhou, Y. Zhang, Y. Qi, H. Zhang, B. Dong, L. Ren, H. Song and L. Xu, A dual-mode foam sensor employing  $\text{Ti}_3\text{C}_2\text{T}_x/\text{In}_2\text{O}_3$  composites for  $\text{NH}_3$  detection with memory function and body movement monitoring for kidney disease diagnosis, *J. Mater. Chem. A*, 2023, **11**, 24299–24310, DOI: [10.1039/D3TA05670H](https://doi.org/10.1039/D3TA05670H).
- 43 M. Luo, X. Huang, D. Xiong, S. Cai, S. Li, Z. Jia and Z. Gao, Fast response/recovery and sub-ppm ammonia gas sensors based on a novel  $\text{V}_2\text{CT}_x/\text{MoS}_2$  composite, *J. Mater. Chem. A*, 2024, **12**, 12225–12236, DOI: [10.1039/D4TA00842A](https://doi.org/10.1039/D4TA00842A).
- 44 L. Hu, R. Xiao, X. Wang, X. Wang, C. Wang, J. Wen, W. Gu and C. Zhu, MXene-induced electronic optimization of metal-organic framework-derived CoFe LDH nanosheet arrays for efficient oxygen evolution, *Appl. Catal., B*, 2021, **298**, 120599, DOI: [10.1016/j.apcatb.2021.120599](https://doi.org/10.1016/j.apcatb.2021.120599).
- 45 Z. Liu, T. He, H. Sun, B. Huang and X. Li, Layered MXene heterostructured with  $\text{In}_2\text{O}_3$  nanoparticles for ammonia sensors at room temperature, *Sens. Actuators, B*, 2022, **365**, 131918, DOI: [10.1016/j.snb.2022.131918](https://doi.org/10.1016/j.snb.2022.131918).
- 46 Q. Li, M. Xu, C. Jiang, S. Song, T. Li, M. Sun, W. Chen and H. Peng, Highly sensitive graphene-based ammonia sensor enhanced by electrophoretic deposition of MXene, *Carbon*, 2023, **202**, 561–570, DOI: [10.1016/j.carbon.2022.11.033](https://doi.org/10.1016/j.carbon.2022.11.033).
- 47 T. He, W. Liu, T. Lv, M. Ma, Z. Liu, A. Vasiliev and X. Li, MXene/ $\text{SnO}_2$  heterojunction based chemical gas sensors, *Sens. Actuators, B*, 2021, **329**, 129275, DOI: [10.1016/j.snb.2020.129275](https://doi.org/10.1016/j.snb.2020.129275).
- 48 H. Tai, Z. Duan, Z. He, X. Li, J. Xu, B. Liu and Y. Jiang, Enhanced ammonia response of  $\text{Ti}_3\text{C}_2\text{T}_x$  nanosheets supported by  $\text{TiO}_2$  nanoparticles at room temperature, *Sens. Actuators, B*, 2019, **298**, 126874, DOI: [10.1016/j.snb.2019.126874](https://doi.org/10.1016/j.snb.2019.126874).
- 49 W. Y. Chen, X. Jiang, S. N. Lai, D. Peroulis and L. Stanciu, Nanohybrids of a MXene and transition metal dichalcogenide for selective detection of volatile organic compounds, *Nat. Commun.*, 2020, **11**, 1302, DOI: [10.1038/s41467-020-15092-4](https://doi.org/10.1038/s41467-020-15092-4).
- 50 Q. T. H. Ta, N. N. Tri and J.-S. Noh, Improved  $\text{NO}_2$  gas sensing performance of 2D  $\text{MoS}_2/\text{Ti}_3\text{C}_2\text{T}_x$  MXene nanocomposite, *Appl. Surf. Sci.*, 2022, **604**, 154624, DOI: [10.1016/j.apsusc.2022.154624](https://doi.org/10.1016/j.apsusc.2022.154624).
- 51 D. Kuang, L. Wang, X. Guo, Y. She, B. Du, C. Liang, W. Qu, X. Sun, Z. Wu, W. Hu and Y. He, Facile hydrothermal synthesis of  $\text{Ti}_3\text{C}_2\text{T}_x\text{-TiO}_2$  nanocomposites for gaseous volatile organic compounds detection at room temperature, *J. Hazard. Mater.*, 2021, **416**, 126171, DOI: [10.1016/j.jhazmat.2021.126171](https://doi.org/10.1016/j.jhazmat.2021.126171).
- 52 M. Liu, J. Ji, P. Song, M. Liu and Q. Wang,  $\alpha\text{-Fe}_2\text{O}_3$  nanocubes/ $\text{Ti}_3\text{C}_2\text{T}_x$  MXene composites for improvement of acetone sensing performance at room temperature, *Sens. Actuators, B*, 2021, **349**, 130782, DOI: [10.1016/j.snb.2021.130782](https://doi.org/10.1016/j.snb.2021.130782).
- 53 B. Sun, H. Lv, Z. Liu, J. Wang, X. Bai, Y. Zhang, J. Chen, K. Kan and K. Shi,  $\text{Co}_3\text{O}_4/\text{PEI}/\text{Ti}_3\text{C}_2\text{T}_x$  MXene nanocomposites for a highly sensitive  $\text{NO}_x$  gas sensor with a low detection limit, *J. Mater. Chem. A*, 2021, **9**, 6335–6344, DOI: [10.1039/D0TA11392A](https://doi.org/10.1039/D0TA11392A).
- 54 X. Tian, L. Yao, X. Cui, R. Zhao, T. Chen, X. Xiao and Y. Wang, A two-dimensional  $\text{Ti}_3\text{C}_2\text{T}_x$  MXene/ $\text{TiO}_2/\text{MoS}_2$  heterostructure with excellent selectivity for the room temperature detection of ammonia, *J. Mater. Chem. A*, 2022, **10**, 5505–5519, DOI: [10.1039/D1TA10773A](https://doi.org/10.1039/D1TA10773A).
- 55 Y. Xia, S. He, J. Wang, L. Zhou, J. Wang and S. Komarneni, MXene/ $\text{WS}_2$  hybrids for visible-light-activated  $\text{NO}_2$  sensing at room temperature, *Chem. Commun.*, 2021, **57**, 9136–9139, DOI: [10.1039/D1CC03474J](https://doi.org/10.1039/D1CC03474J).
- 56 S. Zhang, Y. Ding, Q. Wang and P. Song, MOFs-derived  $\text{In}_2\text{O}_3/\text{ZnO}/\text{Ti}_3\text{C}_2\text{T}_x$  MXene ternary nanocomposites for ethanol gas sensing at room temperature, *Sens. Actuators, B*, 2023, **393**, 134122, DOI: [10.1016/j.snb.2023.134122](https://doi.org/10.1016/j.snb.2023.134122).
- 57 H. Yan, L. Chu, Z. Li, C. Sun, Y. Shi and J. Ma, 2H- $\text{MoS}_2/\text{Ti}_3\text{C}_2\text{T}_x$  MXene composites for enhanced  $\text{NO}_2$  gas sensing properties at room temperature, *Sensors and Actuators Reports*, 2022, **4**, 100103, DOI: [10.1016/j.snr.2022.100103](https://doi.org/10.1016/j.snr.2022.100103).
- 58 H. Peng, J. Yang, C. Lin, L. Qi, L. Li and K. Shi, Gas-sensitive performance of metal-organic framework-derived CuO NPs/ $\text{Ti}_3\text{C}_2\text{T}_x$  MXene heterostructures for efficient  $\text{NO}_2$  detection





- at room temperature, *J. Alloys Compd.*, 2024, **980**, 173657, DOI: [10.1016/j.jallcom.2024.173657](https://doi.org/10.1016/j.jallcom.2024.173657).
- 59 L. Zhao, Y. Zheng, K. Wang, C. Lv, W. Wei, L. Wang and W. Han, Highly Stable Cross-Linked Cationic Polyacrylamide/Ti<sub>3</sub>C<sub>2</sub>T<sub>x</sub> MXene Nanocomposites for Flexible Ammonia-Recognition Devices, *Adv. Mater. Technol.*, 2020, **5**, 2000248, DOI: [10.1002/admt.202000248](https://doi.org/10.1002/admt.202000248).
- 60 Z. Wang, F. Wang, A. Hermawan, Y. Asakura, T. Hasegawa, H. Kumagai, H. Kato, M. Kakihana, J. Zhu and S. Yin, SnO-SnO<sub>2</sub> modified two-dimensional MXene Ti<sub>3</sub>C<sub>2</sub>T<sub>x</sub> for acetone gas sensor working at room temperature, *J. Mater. Sci. Technol.*, 2021, **73**, 128–138, DOI: [10.1016/j.jmst.2020.07.040](https://doi.org/10.1016/j.jmst.2020.07.040).
- 61 J. H. Park, R. H. Hwang, H. C. Yoon and K. B. Yi, Effects of metal loading on activated carbon on its adsorption and desorption characteristics, *J. Ind. Eng. Chem.*, 2019, **74**, 199–207, DOI: [10.1016/j.jiec.2019.03.004](https://doi.org/10.1016/j.jiec.2019.03.004).
- 62 D. Matatagui, A. S. Vidal, I. Gràcia, E. Figueras, C. Cané and J. M. Saniger, Chemoresistive gas sensor based on ZIF-8/ZIF-67 nanocrystals, *Sens. Actuators, B*, 2018, **274**, 601–608, DOI: [10.1016/j.snb.2018.07.137](https://doi.org/10.1016/j.snb.2018.07.137).
- 63 S. J. Kim, H.-J. Koh, C. E. Ren, O. Kwon, K. Maleski, S.-Y. Cho, B. Anasori, C.-K. Kim, Y.-K. Choi, J. Kim, Y. Gogotsi and H.-T. Jung, Metallic Ti<sub>3</sub>C<sub>2</sub>T<sub>x</sub> MXene Gas Sensors with Ultrahigh Signal-to-Noise Ratio, *ACS Nano*, 2018, **12**, 986–993, DOI: [10.1021/acsnano.7b07460](https://doi.org/10.1021/acsnano.7b07460).
- 64 R. S. Mane, S. Pradhan, V. Somkuwar, R. Bhattacharyya, P. C. Ghosh and N. Jha, An electron “donor–acceptor–donor” strategy to activate ZIF-67 as a cathode material for fuel cells and zinc ion hybrid supercapacitor, *React. Chem. Eng.*, 2023, **8**, 891–907, DOI: [10.1039/D2RE00357K](https://doi.org/10.1039/D2RE00357K).

